
Title: Energetic design of grain boundary networks for toughening of nanocrystalline oxides

Authors: Arseniy Bokov, Shenli Zhang, Lin Feng, Shen J. Dillon, Roland Faller, Ricardo H.R. Castro

PII: S0955-2219(18)30303-0
DOI: https://doi.org/10.1016/j.jeurceramsoc.2018.05.007
Reference: JECS 11885

To appear in: *Journal of the European Ceramic Society*

Received date: 5-2-2018
Revised date: 2-5-2018
Accepted date: 8-5-2018

Please cite this article as: Bokov A, Zhang S, Feng L, Dillon SJ, Faller R, Castro RHR, Energetic design of grain boundary networks for toughening of nanocrystalline oxides, *Journal of the European Ceramic Society* (2018), https://doi.org/10.1016/j.jeurceramsoc.2018.05.007

# Energetic design of grain boundary networks for toughening of nanocrystalline oxides

Arseniy Bokov[1], Shenli Zhang[1], Lin Feng[2], Shen J. Dillon[2], Roland Faller[3], and Ricardo H. R. Castro[1,*]

[1]Department of Materials Science and Engineering, University of California, Davis, Davis, California 95616, USA; [2]Department of Materials Science and Engineering, University of Illinois at Urbana-Champaign, Urbana, Illinois 61801, USA; [3]Department of Chemical Engineering, University of California, Davis, Davis, California 95616, USA

* Corresponding author: rhrcastro@ucdavis.edu. Fax: (530) 752-9307. Phone: (530) 752-3724

**Graphical abstract**

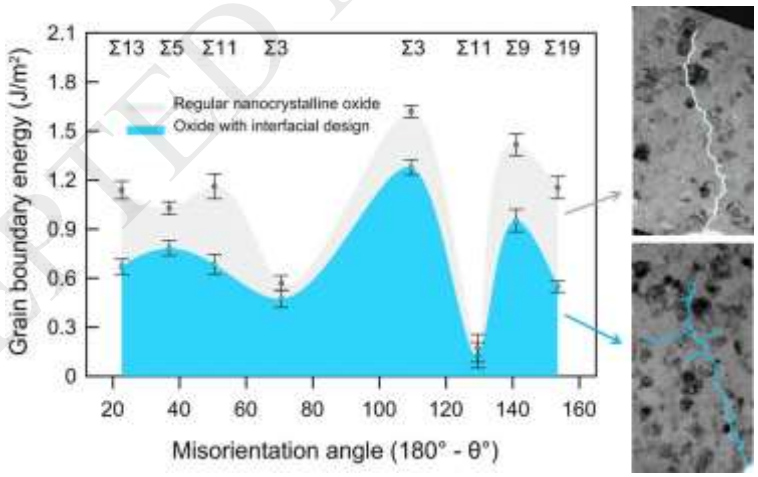


**Abstract:** Improving the mechanical performance of nanocrystalline functional oxides can have major implications for stability and resilience of battery cathodes, development of reliable nuclear

oxide fuels, strong and durable catalytic supports. By combining Monte Carlo simulations, experimental thermodynamics, and in-situ transmission electron microscopy, we demonstrate a novel toughening mechanism based on interplay between the thermo-chemistry of the grain boundaries and crack propagation. By using zirconia as a model material, lanthanum segregation to the grain boundaries was used to increase the toughness of individual boundaries and simultaneously promote a smoother energy landscape in which cracks experience multiple deflections through the grain boundary network, ultimately improving fracture toughness.

**Keywords:** grain boundary, segregation, fracture toughness, nanocrystalline ceramics, zirconia

## 1. Introduction

The mechanical performance of many functional oxides is limited due to the intrinsic brittleness resulting from the relatively fast crack nucleation and propagation through the material, which causes failure even at low impact energies. An effective mechanism designed to increase toughness in oxides is the transformation toughening in zirconium dioxide ($ZrO_2$) [1]. Crack propagation in this material triggers a suppressed phase transition, causing a local volumetric expansion and arresting crack motion. While being quite effective, this mechanism only exists in $ZrO_2$-based materials or others few oxides that show similar phase stability diagrams. As for the rest of the oxides, a possible solution to increase toughness is the design of composite materials, such as host matrices with a random distribution or layered arrangement of reinforcing species. The former relies on the crack-bridging effect of some compounds with superior tensile strength, such as SiC nanoparticles or carbon nanotubes [2,3]. The latter uses layered configurations to resist fracturing since cracks can experience multiple deflections going from one layer to another [4]. Although the formation of composites is a flexible approach, a significant amount of secondary compounds

strongly affects functional properties of the host, such as light transmission and mobility of charged species [5,6].

As the grain size decreases to the nanoscale, new opportunities for functional oxide materials emerge, such as increased charge-discharge rates in lithium battery cathodes [7–9], and improved radiation tolerance in nuclear materials [10,11]. Some theoretical works have also predicted new mechanisms of toughening based on sliding of nanosized grains. As a result of new deformation modes [12–14], stress fields would potentially compensate external stresses near the crack tips and hinder their movement. However, those effects have not been experimentally observed in oxides, implying the validity of the alternate hypothesis, in which the lack of perfect atomic arrangement at the grain boundaries leads to weaker bonding/coordination. A large number of interfaces therefore defines the overall (limited) mechanical strength of nanocrystalline oxides by acting as regions of easy crack nucleation and propagation [15,16].

While the increase in bond strength and bonding coordination at the grain boundaries could potentially increase toughness [17], similarly to what has been proposed for thermal creep [18]; crack deflection by forming composites can lead to much larger improvements. In this approach, the angle of crack deflection directly dictates the increase in toughness. If one can induce cracking on directions of non-maximum energy, then an apparent increase of the fracture toughness will be achieved [19]. Since deflection can be induced by any discontinuity, one may observe an inherent crack deflection pathway in the context of nanomaterials, which is the existing grain boundary network itself. Such network is, however, generally ineffective for deflection because of the random grain boundary distribution found in typical polycrystalline materials, i.e. co-existence of high energy and low energy boundaries. The high excess energy boundaries tend to be mechanically weaker than the low energy ones due the existing large density of uncompensated chemical bonds and coordination [20]. It is therefore intuitive to say that low excess energies correspond to

mechanically stronger (or more accurately, tougher, as one is talking about the energy till failure) boundaries because of their intrinsic stability. Likely intuitive, if the network is a combination of both, crack-tips will more easily propagate along boundaries with higher excess energy and "avoid" the ones with low excess energy, resulting in fairly straight and unbranched cracks typical of brittle behavior [21].

To induce crack deflection in the existing grain boundary network, we propose the hypothesis that all grain boundaries should be similar in terms of their excess energies. As a result, a stochastic deflection of crack path will be achieved – ultimately increasing fracture toughness. Such mechanism, however, would only work if grain boundaries were generally made stronger rather than the opposite [22]. It can minimize the energetic discontinuities that grain boundaries constitute in the system, and thus disabling low critical strain-energy release rate boundaries.

Leveling off the energy landscape in the grain boundary network has just become achievable based on recent advancements on the control of the thermodynamics of interfaces [23,24]. Grain boundary energies ($\gamma_{gb}$) can be chemically modified through segregation of dopants, following the simplified Gibbs adsorption equation for low concentrations:

$$\gamma_{gb} = \gamma_0 - \Gamma_B\left(RT \ln X_B^{bulk} - \Delta H_{seg}\right) \quad (1)$$

Here, $\gamma_0$ is the grain boundary energy of the undoped grain boundary, $\Gamma_B$ is the solute excess at the grain boundary, $\Delta H_{seg}$ is the enthalpy of segregation, and $X_{Bbulk}$ the bulk solute content [24]. If the enthalpy of segregation is favorable, the grain boundary energy decreases, becoming more energetically stable. Such favorable segregation enthalpy has been observed in oxides, for instance, when doped with rare-earth elements or transition metals [25,26]. Noteworthy, the segregation enthalpy is a function of grain boundary orientation and its intrinsic (dopant free) energy. High energy boundaries typically demonstrate a more favorable enthalpy of segregation, while low energy

boundaries are inherently more stable and not prone to accommodate dopants [27]. This natural anisotropic interaction of dopants and boundaries could be directly used to homogenize the energetic landscape across the grain boundary network.

## 2. Methods and materials

### 2.1 Monte Carlo simulations

In this study, the potential effect of ion segregation in a model oxide system was investigated using Monte Carlo (MC) simulations. The simulations were performed for cubic $ZrO_2$ stabilized by 10 mol.% of $Y_2O_3$ (10YSZ), commonly used for solid electrolytes or thermal barrier coating due to the absence of phase transformations in a wide range of grain sizes, temperatures, and stresses [28]. The grain boundaries of this material were modeled in different crystallographic orientations with and without La as a dopant, which was previously shown to decrease the average grain boundary energy in zirconia [29].

Initially, the structures of the pure $ZrO_2$ were built and relaxed using a gradient descent algorithm implemented in the LAMMPS code [30]. Then, the formation of a solid solution of $ZrO_2$ with $Y_2O_3$ as well as the doping with La were performed by random substitution of cations and following equilibration using the TOWHEE software [31]. The interaction between anions and cations was treated as fully ionic, modeled by a short-range Born-Mayer-Buckingham potential with the cutoff distance of 10 Å, and the long-range Coulomb potential. This potential model has been proven to reasonably reproduce the cubic structure of YSZ as well as other oxide compounds [32].

The MC simulations were carried out under NVT conditions (constant atom number, constant volume and constant temperature, T = 300 K) for $10^8$ steps to ensure fully equilibration. Two modes of motion were considered: swapping for cations only, and translation for all ions. For each simulation step, the energy of the configuration was calculated and the new configuration accepted

with probability of the minimum value in (1, exp(-$\Delta E/k_B T$)). Here $\Delta E$ is the energy difference before and after MC trial moves, $k_B$ is the Boltzmann's constant and T is temperature.

The scope of this simulation part in this study was limited to the most common grain boundaries found in YSZ ceramic (Table 1). For instance, the experimental investigations are reported for Σ5 and Σ13 boundaries with [100] tilt [33,34] as well as for Σ3, Σ9 and Σ11 with [110] tilt [35]. For each boundary geometry and composition, 3 independent configurations were simulated in our work. The composition of the pristine boundary was set to $ZrO_2$ + 10 mol.% $Y_2O_3$ (10YSZ), while 1.5 mol. % of $Y_2O_3$ was substituted by $La_2O_3$ in the doped case, i.e. $ZrO_2$ + 8.5mol.% $Y_2O_3$ + 1.5 mol.% $La_2O_3$ (1.5La8.5YSZ). Although Σ19 boundary has not been experimentally studied in the literature, this geometry was also found stable in our simulations. The grain boundary structures were formed by rotating two grains about the tilt direction set as *z* axis so that *x* and *z* axes form the grain boundary plane with *y* axis perpendicular to the this plane. Overlapping atoms (<0.3 Å) due to rotation were not taken into account. Periodic boundary conditions were applied in all three directions, and the length of simulation box was set in such a way that ensures an integer multiples the lattice constant.

Additionally, the reference structures without grain boundary were simulated for both compositions. The values of grain boundary energy were calculated as difference in internal energy between the grain boundary configurations and the reference structures without boundary. Each value represents the average of 20 data points uniformly sampled at different times of the equilibration process. The obtained values were additionally averaged with other independent configurations. The entropy contribution to the grain boundary energy was negligible due to temperature of simulations. The contribution of volume expansion was also neglected since it only accounted for 0.2% of the total energy.

### 2.2 Synthesis of nanocrystalline powders

The nanocrystalline powders of the pure and La-doped YSZ were synthesized by reverse co-precipitation [36]. Required proportions of the starting reagents zirconium(IV) oxynitrate hydrate (Sigma Aldrich, 99%), yittrium(III) nitrate hexahydrate (Alfa Aesar, 99.9%), and lanthanum(III) nitrate hexahydrate (Alfa Aesar, 99.9%) were mixed with deionized water to form 0.75M aqueous solutions. The concentration of dopant was set in a similar way as for modeling: 0.5, 1.0 or 1.5 mol. % of $Y_2O_3$ was substituted by $La_2O_3$. The dissolved nitrates were slowly dripped into 5M excess solution of ammonium hydroxide which resulted in a rapid precipitation. The precipitates were washed after centrifuging three times with ethanol and then dried in a drying oven at 80°C for 48 h. The obtained precursors were crushed into fine powders and calcined at 450°C in ambient air to form nanocrystalline oxides. After calcination all powders were degassed and stored in a glovebox to ensure moisture-free particles surface.

### 2.3 Sintering of dense samples from powders

Fully dense ceramics were produced from the synthesized powders using high-pressure spark plasma sintering of on SPS model 825S (Syntex, Japan). These powders were loaded in the diamond-silicon carbide composite inner die under dry nitrogen atmosphere. This die was then placed into the outer graphite die using the composite spacers of the above-mention composition. The composite parts were used to apply high pressure whereas the outer graphite parts were needed to conduct a pulsed current. The ceramic samples were sintered in vacuum at 1.7 GPa pressure in 960-1070°C range of temperatures without dwell time. After sintering all samples were reoxidized for 1 h under ambient air at 150°C below sintering temperature. The average grain size of the resulting ceramic pellets was about 19.5±1.5 nm, ensuring very large grain boundary areas.

### 2.4 Experimental measurements of grain boundary energy

The average grain boundary energy of the sintered samples was analyzed using Differential Scanning Microcalorimetry (DSC) on Netzsch DSC404 (Netzsch GmbH, Germany). This technique is thoroughly described elsewhere [37], so the following notes only reflect the most essential parts of these measurements. In a typical procedure, ceramic pellets were exposed at 200°C for 30 min to clean the surface from moisture. Then, samples were heated up in argon (20°C/min) to 1150°C followed by 20 min holding to activate grain growth. Since no phase transformation or redox reaction was present, the released heat was exclusively related to the decrease of the grain boundary area (surface area is relatively small for nanocrystalline samples). The grain boundary energy was then calculated by dividing the released heat by the change of the grain boundary area. The X-Ray powder diffraction (XRD) and SEM were used to determine the initial and final grain sizes (before and after the heat release) in order to calculate the change in the grain boundary area the using geometrical assumption grain are tetrakaidekahedra [38], which as confirmed to be a resonable assumption when observing grains under the microscope. X-day diffraction was performed on Bruker-AXS D8 Advance diffractometer (Bruker-AXS, Inc.) using a copper radiation source operated at 40 kV and 40 mA. The crystallite size of the sintered samples was determined from the pattern refinement using the JADE 6.1 (MDI) software.

### 2.5 Measurements of macroscopic fracture toughness

The macroscopic fracture toughness was measured from the hardness impressions left by a Vickers indenter (Mitutoyo HM-220A) as the average between three equations: Lankford [39], Laugier [40], and Shetty-Wright-Mincer-Clauer [41]. These equations were proven to provide the smallest deviation from fracture toughness obtained by other techniques [42,43]. Rather than relying on optical images, the obtained hardness impressions were imaged on Scanning Electron

Microscope (SEM) FEI Nova NanoSEM430 using backscattered electrons, 5 kV accelerating voltage and 6.5 mm working distance. About 130 impressions were used for toughness calculations: roughly 32-33 for each composition including 11-12 for each indentation load (30 gf, 40 gf, 50 gf).

### 2.6 TEM sample preparation

The sintered ceramic samples were mechanical polished to a thickness of about 15 μm using 1 μm diamond lapping films. Notched cantilever specimens for in-situ transmission electron microscopy (TEM) mechanical testing were prepared using focused ion beam milling (FEI Helios). Cantilevers were prepared to be about 7 μm long, 2 μm tall, and 50-500 nm thick, with 1.5 μm V-shaped notches located in the center. Thin samples were utilized for in-situ imaging, while thick samples were used to obtain mechanical properties. Final thinning was performed using 5 keV $Ga^{+}$ ions.

### 2.7 In-situ TEM mechanical testing

In-situ TEM nanomechanical testing was performed using a Hysitron PI-95 picoindentor in a JEOL 2010 $LaB_6$ TEM (Fig. 1). Samples were loaded at a constant displacement rate of 1 nm $s^{-1}$. The specimen and loading geometries were simulated in ABAQUS, and fracture toughness values were calculated using the J-integral method. Several samples of each composition were tested to obtain mean values and ensure reproducibility in calculated mechanical properties and crack morphologies.

## 3. Results and discussion

The results of MC simulation for the case of Σ13 boundaries with and without La, as well as the for the reference bulk phase of 10YSZ are shown in Fig. 2. The actual atomic configurations can be seen in Fig. 2A-C, while the distribution of potential energies in the crystalline lattices for corresponding structures are represented in Fig. 2D-I. The energy maps for the anionic sublattice are relatively uniform for all structures (Fig. 2D-F) indicating that dopant atoms do not destabilize oxygen. However, the overall energy landscape is much more complicated for the cationic sublattice. The existence of a grain boundary in 10YSZ creates high energy lattice sites (Fig. 2H) as compared to the bulk phase (Fig. 2G), which implies a relative mechanical weakness of such interface. The energy map for the structure with a segregated dopant is more homogenous, with narrower regions of higher energy (Fig. 2I) and expectedly higher mechanical stability as compared to the undoped boundary.

A distinct behavior of the cationic sublattice can be understood from the radial density functions which represent the number of neighbors at a specific distance. As it can be seen in Fig. 3A, doping does not increase the total number of bonds at the boundary as it has been suggested to occur in Y-doped alumina [18]. However, a longer bond length for La-O interaction is observed as compared to Zr-O or Y-O (Fig. 3B) similarly to $Al_2O_4$ with Lu doping [44]. As a result, longer La-O bonds allow for the redistribution of oxygen atoms so that they can occupy sites which are energetically more favorable for Zr or Y. Such energetic stabilization at the atomic level results in a significant reduction of grain boundary excess energies. Although the actual decrease in grain boundary energies (Fig. 4A) varies with the geometry of grain boundaries, the high energy boundaries are more affected by the presence of dopant, expectedly showing a more pronounced energy decrease. This causes an overall equalization of the existing grain boundaries in terms of energy, along with toughening of individual boundaries.

For the experimental verification of the suggested concept, the grain boundary energy was experimentally measured by subjecting the fully dense samples of the pure and La-doped YSZ to DSC analyses. Fig. 4B shows the characteristic exothermic peaks which are associated with the release of the excess grain boundary energy. More specifically, the increase in the dopant concentration from 0 to 1.5 mol. % of La leads to a significant reduction of the area under the DSC curve. This is a direct indication of the decrease in (average) grain boundary energy due to segregation of La, which is consistent with simulations. The actual grain boundary energies were calculated by quantifying the grain boundary area before and after the exothermic peak and attributing the integral energy to the grain boundary area evolution. This can only be made because samples are pore-free (~100% of theoretical density, no surface area available) and no parallel reactions, such as reductions or decompositions are observed. The values of energies are shown in Fig. 4C for the different La contents.

Systematic diamond indentations were performed to understand how well the decrease in total energy and energy anisotropy translates into macroscopic mechanical properties. The measured fracture toughness plotted versus the average grain boundary energy (measured by DSC) in Fig. 4C shows a direct correlation between these properties. The undoped 10YSZ shows fracture toughness of 1.74 $MPa.m^{1/2}$, which is consistent with the data found in the literature for the large grained cubic zirconia [45], indicating that nanosized grains alone do not contribute to toughening. On the other hand, the addition of lanthanum causes a remarkable increase in toughness (+20% for 1.5 mol. % of La) with respect to the pure nanocrystalline zirconia. While it is tempting to associate this increase to the grain boundary energy decrease alone based on Fig. 3C, the total energy decrease (-0.4 $J.m^{-2}$) is rather small as compared to the total energy required for fracture in zirconia (12 $J.m^{-2}$) [45], implying an additional mechanism is activated by La doping.

The following investigations with in-situ TEM fracture tests showed additional details of the crack movement and revealed the role of the grain boundary energy distribution. The TEM snapshots demonstrating evolution of crack propagation in the 10YSZ and 1.5La8.5YSZ compositions are shown in Fig. 5A-B. The first observation is that no grain sliding is seen, as previously suggested to occur and to be responsible for improved toughness in nanocrystalline ceramics [14]. Without active toughening mechanism, 10YSZ shows a single crack propagating through the grain boundaries (Fig. 5A, Video 1), leading to relatively low toughness. This situation is consistent with the existence of a large population of high energy (low toughness) grain boundaries in the network, which induces high energy-release rates. For La-doped YSZ, grain sliding is also not observed, but crack path experience several deflections to multiple independent grain boundaries in the network (Fig. 5B, Video 2), which is reflected by the apparent increase in toughness.

The values of fracture toughness measured from the in-situ TEM analysis showed an increase of about 20% which coincides with the macroscopic measurements despite the small dimensions of the TEM sample. Noteworthy, from the in-situ TEM videos, the ratio of total crack length to projected crack length is 1.13 and 1.90 for 10YSZ and La-doped YSZ, respectively (Fig. 6A-B). A significant difference in the crack patterns can also be seen from macroscopic impressions created by indentations with diamond pyramid (Fig. 6B-C). Similarly to in-situ TEM tests, cracks in 10YSZ are rather straight while more curved cracks with visible branching are seen for the La-doped ones.

The effectiveness of this new toughening mechanism relies on the ‘activation’ of crack paths by decreasing the energy difference between each individual grain boundary in the network. In the proposed model example, La showed anisotropic segregation and cause multiple crack deflections, as observed in the in-situ TEM study. This mechanism is therefore fundamentally different from classical dispersion or precipitation toughening in which the onset of crack branching is driven by

the residual stresses on the interface of the reinforcement particles or fibers [19], and can be used in the design of single-phase functional oxides with enhanced toughness.

An important clarification is that the proposed chemical segregation discussed here is very distinct from the formation of separate second phases as intergranular films. The dopants in our study occupy the lattice sites of the host crystal (YSZ in this case) yet staying mostly at the grain boundaries, resulting in an interface excess that reduces the overall grain boundary energy. This is a necessary condition for the design and differs from intergranular films [46], which constitute an additional crystalline or amorphous phase decorating the grain boundaries [22]. The absence of second phases can be seen in Fig. 7 which shows XRD profiles showing only with the characteristic zirconia cubic fluorite structure. The phase purity can be also confirmed with the physical appearance of sintered ceramics, such that 10YSZ and 1.5La8.5YSZ pellets both demonstrate the same level of optical transparency under illumination with daylight (Fig. 7). This would not be possible if second phases were present due to the difference in refractive index of the potential second phase (according to phase diagram) lanthanum zirconate and the host zirconia lattice [47].

It is also worth mentioning that second phases are likely expected to lower the grain boundary toughness because of the structural and/or chemical mismatch at the interface regions [48]. Although these can enable crack branching or deflection, intergranular cracking is relatively easy and lowers overall the toughness. In our work, grain boundary toughness was increased and at the same time crack deflection is promoted, creating an unpreceded and powerful mechanism. Within the context of grain boundary excesses, it is likely that local structures, such as grain boundary complexions, can be formed [49]. These are results of local configuration of ions along the boundaries which would potentially affect grain boundary local strength [50], but more studies are needed to allow a more comprehensive understanding.

## 4. Conclusions

The obtained results set the fundaments of a new toughening mechanism for nanocrystalline oxides. Addressing the grain boundaries as thermodynamically tunable parameters, one may increase local strength, represented by lowering grain boundary excess energies, while decreasing the anisotropy in the existing populations of grain boundaries. Together they provide superior fracture toughness by deflecting the propagation of cracks. The flexibility of this approach provides design opportunities in single-phased ceramics since toughness can be controlled without significant volumetric or chemical changes. Our experimental work on La-doped cubic zirconia is an example to demonstrate the potential of the approach that may be applied to other systems, dense or partially sintered, in particular functional oxides.

## Supplementary information

Videos 1 and 2. In-situ TEM of crack propagation in 10YSZ and 1.5La8.5YSZ (available on the webpage of this journal article).

## Acknowledgment

The experimental work was financially supported by the Army Research Office Grant W911NF-17-1-0026 and is acknowledged by RC and AB. U.S. Department of Energy, Office of Nuclear Energy, Nuclear Energy University Program under Grant DE-NE0000704 is acknowledged for supporting SZ and RF. LF and SJD were supported by National Science Foundation Grant No. 1254406.

## References

[1] R.H.J. Hannink, P.M. Kelly, B.C. Muddle, Transformation Toughening in Zirconia-Containing Ceramics, J. Am. Ceram. Soc. 83 (2004) 461–487. doi:10.1111/j.1151-

2916.2000.tb01221.x.

[2] T. Ohji, Y.-K. Jeong, Y.-H. Choa, K. Niihara, Strengthening and Toughening Mechanisms of Ceramic Nanocomposites, J. Am. Ceram. Soc. 60 (1998) 1453–1460. doi:10.1111/j.1151-2916.1998.tb02503.x.

[3] G.-D. Zhan, J.D. Kuntz, J. Wan, A.K. Mukherjee, Single-wall carbon nanotubes as attractive toughening agents in alumina-based nanocomposites, Nat. Mater. 2 (2003) 38–42. doi:10.1038/nmat793.

[4] P.E.D. Morgan, D.B. Marshall, Ceramic Composites of Monazite and Alumina, J. Am. Ceram. Soc. 78 (1995) 1553–1563. doi:10.1111/j.1151-2916.1995.tb08851.x.

[5] J. Miller, I. Reimanis, W. Miao, J. Salem, Mechanical and optical properties in precipitated regions of alumina-rich magnesium aluminate spinel, Int. J. Appl. Ceram. Technol. 14 (2017) 236–244. doi:10.1111/ijac.12644.

[6] M. Mori, T. Abe, H. Itoh, O. Yamamoto, Y. Takeda, T. Kawahara, Cubic-stabilized zirconia and alumina composites as electrolytes in planar type solid oxide fuel cells, Solid State Ionics. 74 (1994) 157–164. doi:10.1016/0167-2738(94)90206-2.

[7] R. Malik, D. Burch, M. Bazant, G. Ceder, Particle Size Dependence of the Ionic Diffusivity, Nano Lett. 10 (2010) 4123–4127. doi:10.1021/nl1023595.

[8] Y. Zhao, L. Peng, B. Liu, G. Yu, Single-Crystalline $LiFePO_4$ Nanosheets for High-Rate Li-Ion Batteries, Nano Lett. 14 (2014) 2849–2853. doi:10.1021/nl5008568.

[9] H. Liu, M. Wolf, K. Karki, Y.-S. Yu, E.A. Stach, J. Cabana, et al., Intergranular Cracking as a Major Cause of Long-Term Capacity Fading of Layered Cathodes, Nano Lett. 17 (2017) 3452–3457. doi:10.1021/acs.nanolett.7b00379.

[10] S. Dey, J.W. Drazin, Y. Wang, J.A. Valdez, T.G. Holesinger, B.P. Uberuaga, et al., Radiation Tolerance of Nanocrystalline Ceramics: Insights from Yttria Stabilized Zirconia, Sci. Rep. 5

(2015) 7746. doi:10.1038/srep07746.

[11] I.J. Beyerlein, A. Caro, M.J. Demkowicz, N.A. Mara, A. Misra, B.P. Uberuaga, Radiation damage tolerant nanomaterials, Mater. Today. 16 (2013) 443–449. doi:10.1016/j.mattod.2013.10.019.

[12] Y. Mo, I. Szlufarska, Simultaneous enhancement of toughness, ductility, and strength of nanocrystalline ceramics at high strain-rates, Appl. Phys. Lett. 90 (2007) 181926. doi:10.1063/1.2736652.

[13] I.A. Ovid'ko, A.G. Sheinerman, Micromechanisms for improved fracture toughness in nanoceramics, Rev. Adv. Mater. Sci. 29 (2011) 105–125.

[14] I.A. Ovid'ko, Micromechanics of fracturing in nanoceramics, Philos. Trans. R. Soc. A Math. Phys. Eng. Sci. 373 (2015) 20140129–20140129. doi:10.1098/rsta.2014.0129.

[15] R. Birringer, Nanocrystalline materials, Mater. Sci. Eng. A. 117 (1989) 33–43. doi:10.1016/0921-5093(89)90083-X.

[16] I.A. Ovid'ko, Review on the fracture processes in nanocrystalline materials, J. Mater. Sci. 42 (2007) 1694–1708. doi:10.1007/s10853-006-0968-9.

[17] L. Wu, S. Dey, J. Mardinly, M. Hasan, R.H.R. Castro, Thermodynamic Strengthening of Heterointerfaces in Nanoceramics, Chem. Mater. 28 (2016) 2897–2901. doi:10.1021/acs.chemmater.6b00074.

[18] J.P. Buban, K. Matsunaga, J. Chen, N. Shibata, W.Y. Ching, T. Yamamoto, et al., Grain Boundary Strengthening in Alumina by Rare Earth Impurities, Science (80-. ). 311 (2006) 212–215. doi:10.1126/science.1119839.

[19] K.T. Faber, A.G. Evans, Crack deflection processes—I. Theory, Acta Metall. 31 (1983) 565–576. doi:10.1016/0001-6160(83)90046-9.

[20] S. Tsurekawa, T. Tanaka, H. Yoshinaga, Grain boundary structure, energy and strength in

molybdenum, Mater. Sci. Eng. A. 176 (1994) 341–348. doi:10.1016/0921-5093(94)90997-0.

[21] T. Watanabe, S. Tsurekawa, Toughening of brittle materials by grain boundary engineering, Mater. Sci. Eng. A. 387–389 (2004) 447–455. doi:10.1016/j.msea.2004.01.140.

[22] C.L. Conner, K.T. Faber, Segregant-enhanced fracture in magnesium oxide, J. Mater. Sci. 25 (1990) 2737–2742. doi:10.1007/BF00584873.

[23] R.H.R. Castro, On the thermodynamic stability of nanocrystalline ceramics, Mater. Lett. 96 (2013) 45–56. doi:10.1016/j.matlet.2013.01.007.

[24] T. Chookajorn, H. a Murdoch, C. a Schuh, Design of Stable Nanocrystalline Alloys, Science (80-. ). 337 (2012) 951–954. doi:10.1126/science.1224737.

[25] M.M. Hasan, P.P. Dholabhai, S. Dey, B.P. Uberuaga, R.H.R. Castro, Reduced grain boundary energies in rare-earth doped $MgAl_2O_4$ spinel and consequent grain growth inhibition, J. Eur. Ceram. Soc. 37 (2017) 4043–4050. doi:10.1016/j.jeurceramsoc.2017.04.073.

[26] L. Wu, J.A. Aguiar, P.P. Dholabhai, T. Holesinger, T. Aoki, B.P. Uberuaga, et al., Interface Energies of Nanocrystalline Doped Ceria: Effects of Manganese Segregation, J. Phys. Chem. C. 119 (2015) 27855–27864. doi:10.1021/acs.jpcc.5b09255.

[27] G.D. West, J.M. Perkins, M.H. Lewis, Characterisation of fine-grained oxide ceramics, J. Mater. Sci. 39 (2004) 6687–6704. doi:10.1023/B:JMSC.0000045600.77776.08.

[28] J.W. Drazin, R.H.R. Castro, Phase Stability in Nanocrystals: A Predictive Diagram for Yttria-Zirconia, J. Am. Ceram. Soc. 98 (2015) 1377–1384. doi:10.1111/jace.13504.

[29] S. Dey, C. Chang, M. Gong, F. Liu, R.H.R. Castro, Grain growth resistant nanocrystalline zirconia by targeting zero grain boundary energies, J. Mater. Res. 30 (2015) 2991–3002. doi:10.1557/jmr.2015.269.

[30] S. Plimpton, Fast Parallel Algorithms for Short-Range Molecular Dynamics, J. Comput. Phys. 117 (1995) 1–19. doi:10.1006/jcph.1995.1039.

[31] M.G. Martin, MCCCS Towhee: a tool for Monte Carlo molecular simulation, Mol. Simul. 39 (2013) 1212–1222. doi:10.1080/08927022.2013.828208.

[32] M. Zacate, L. Minervini, D.J. Bradfield, R.W. Grimes, K.E. Sickafus, Defect cluster formation in $M_2O_3$-doped cubic $ZrO_2$, Solid State Ionics. 128 (2000) 243–254. doi:10.1016/S0167-2738(99)00348-3.

[33] Y. Lei, Y. Ito, N.D. Browning, T.J. Mazanec, Segregation Effects at Grain Boundaries in Fluorite-Structured Ceramics, J. Am. Ceram. Soc. 85 (2002) 2359–2363. doi:10.1111/j.1151-2916.2002.tb00460.x.

[34] E.C. Dickey, X. Fan, S.J. Pennycook, Structure and Chemistry of Yttria-Stabilized Cubic-Zirconia Symmetric Tilt Grain Boundaries, J. Am. Ceram. Soc. 84 (2004) 1361–1368. doi:10.1111/j.1151-2916.2001.tb00842.x.

[35] N. Shibata, F. Oba, T. Yamamoto, Y. Ikuhara, Structure, energy and solute segregation behaviour of [110] symmetric tilt grain boundaries in yttria-stabilized cubic zirconia, Philos. Mag. 84 (2004) 2381–2415. doi:10.1080/14786430410001693463.

[36] M.J. Mayo, D.C. Hague, D.-J. Chen, Processing nanocrystalline ceramics for applications in superplasticity, Mater. Sci. Eng. A. 166 (1993) 145–159. doi:10.1016/0921-5093(93)90318-9.

[37] D. V Quach, R.H.R. Castro, Direct measurement of grain boundary enthalpy of cubic yttria-stabilized zirconia by differential scanning calorimetry, J. Appl. Phys. 112 (2012) 83527. doi:10.1063/1.4761992.

[38] C.D. Terwllliger, Y.-M. Chiang, Measurements of Excess Enthalpy in Ultrafine-Grained Titanium Dioxide, J. Am. Ceram. Soc. 78 (1995) 2045–2055. doi:10.1111/j.1151-2916.1995.tb08616.x.

[39] J. Lankford, Indentation microfracture in the Palmqvist crack regime: implications for fracture toughness evaluation by the indentation method, J. Mater. Sci. Lett. 1 (1982) 493–495.

doi:10.1007/BF00721938.

[40] M.T. Laugier, New formula for indentation toughness in ceramics, J. Mater. Sci. Lett. 6 (1987) 355–356. doi:10.1007/BF01729352.

[41] D.K. Shetty, I.G. Wright, P.N. Mincer, A.H. Clauer, Indentation fracture of WC-Co cermets, J. Mater. Sci. 20 (1985) 1873–1882. doi:10.1007/BF00555296.

[42] C.B. Ponton, R.D. Rawlings, Vickers indentation fracture toughness test Part 1 Review of literature and formulation of standardised indentation toughness equations, Mater. Sci. Technol. 5 (1989) 865–872. doi:10.1179/mst.1989.5.9.865.

[43] C.B. Ponton, R.D. Rawlings, Vickers indentation fracture toughness test Part 2 Application and critical evaluation of standardised indentation toughness equations, Mater. Sci. Technol. 5 (1989) 961–976. doi:10.1179/mst.1989.5.10.961.

[44] H. Yoshida, Y. Ikuhara, T. Sakuma, M. Sakurai, E. Matsubara, X-ray absorption fine-structure study on the fine structure of lutetium segregated at grain boundaries in fine-grained polycrystalline alumina, Philos. Mag. 84 (2004) 865–876. doi:10.1080/14786430310001638753.

[45] A. Selçuk, A. Atkinson, Strength and Toughness of Tape-Cast Yttria-Stabilized Zirconia, J. Am. Ceram. Soc. 83 (2000) 2029–2035. doi:10.1111/j.1151-2916.2000.tb01507.x.

[46] R.S. Jupp, D.F. Stein, D.W. Smith, Observations on the effect of calcium segregation on the fracture behaviour of polycrystalline alumina, J. Mater. Sci. 15 (1980) 96–102. doi:10.1007/BF00552432.

[47] S.M. Lakiza, V.P. Red'ko, L.M. Lopato, Triangulation and Liquidus Surface in the $Al_2O_3$ - $ZrO_2$- $La_2O_3$ Phase Diagram, Powder Metall. Met. Ceram. 41 (2002) 627–636. doi:10.1023/A:1022940421535.

[48] M. Rubat du Merac, H.-J. Kleebe, M.M. Müller, I.E. Reimanis, Fifty Years of Research and

Development Coming to Fruition; Unraveling the Complex Interactions during Processing of Transparent Magnesium Aluminate ($MgAl_2O_4$) Spinel, J. Am. Ceram. Soc. 96 (2013) 3341–3365. doi:10.1111/jace.12637.

[49] P.R. Cantwell, M. Tang, S.J. Dillon, J. Luo, G.S. Rohrer, M.P. Harmer, Grain boundary complexions, Acta Mater. 62 (2014) 1–48. doi:10.1016/j.actamat.2013.07.037.

[50] L. Feng, R. Hao, J. Lambros, S.J. Dillon, The influence of dopants and complexion transitions on grain boundary fracture in alumina, Acta Mater. 142 (2018) 121–130. doi:10.1016/j.actamat.2017.09.002.

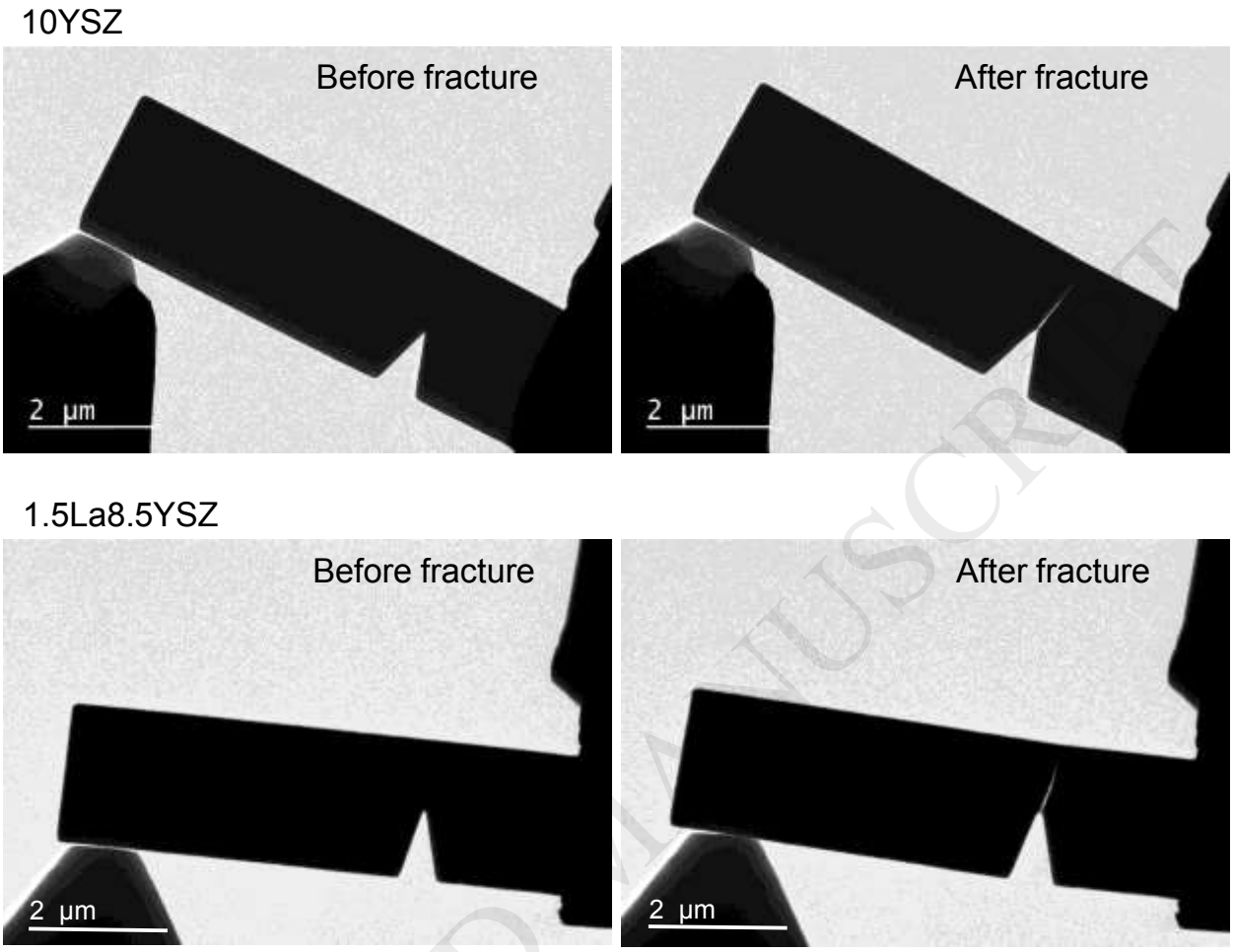


**Fig. 1.** The configuration of in-situ TEM fracture tests utilized in this study. The indenter was used to initiate fracture at the v-shaped notch.

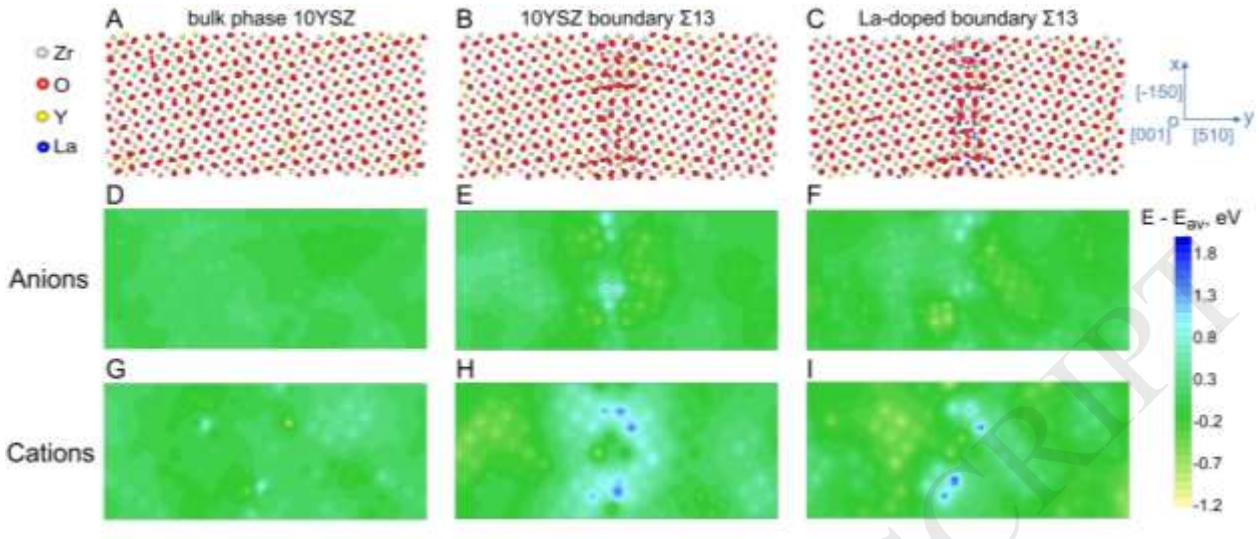


**Fig. 2.** The atomic configuration of the 10YSZ bulk phase (A), Σ13 boundary in 10YSZ (B), and Σ13 boundary in 1.5La8.5YSZ (C) produced by Monte Carlo simulations. The energy distribution maps represent the deviation of the potential energy from the average value in the anionic (D, E, F) and cationic (G, H, I) sublattices. The average potential energies for all types of ions in each structure are reported in Table 2.

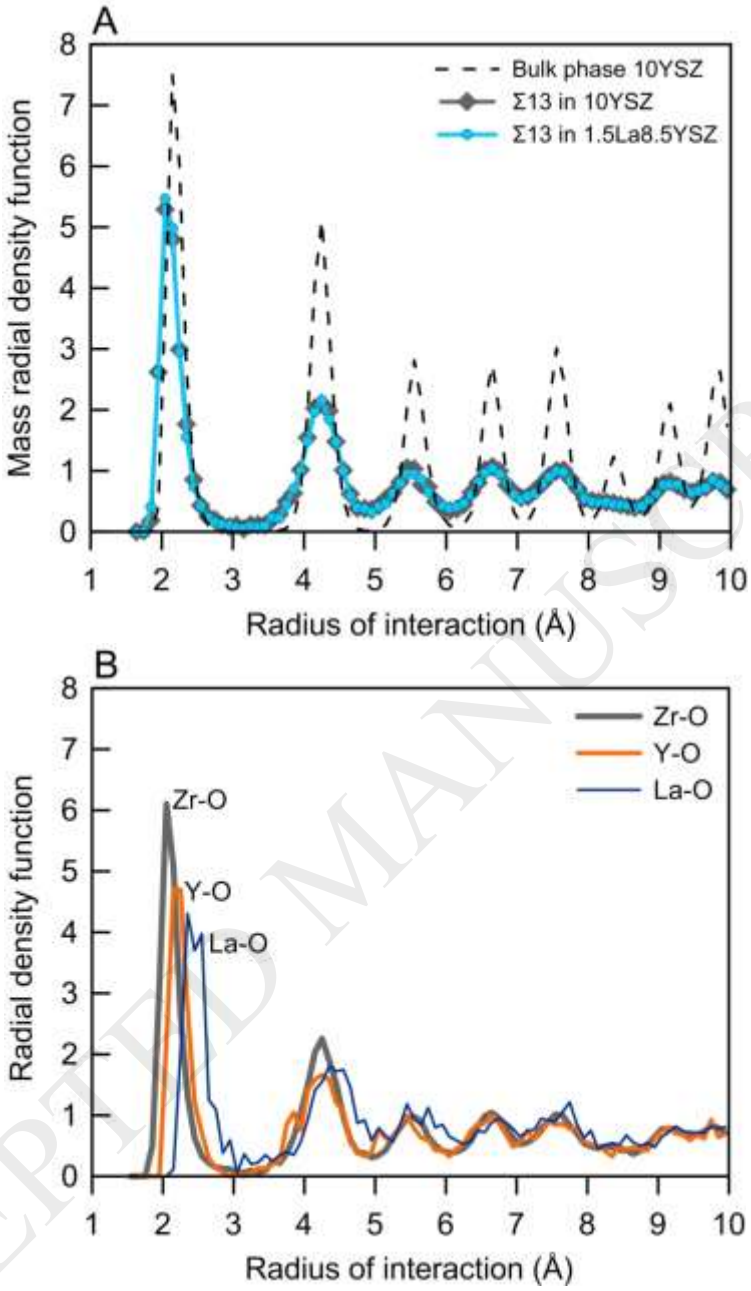


**Fig. 3.** Mass radial density function for the reference bulk phase of 10YSZ and for Σ13 boundaries of 10YSZ and 1.5La8.5YSZ (A). Radial density functions for the pair interactions of Zr-O, Y-O and La-O in the core region of Σ13 (B). The width of the core region is taken as 12 Å. The bond length of Zr and Y with the 1-st nearest oxygen atoms is 2.05 Å and 2.15 Å respectively. The bond length for La-O is longer, demonstrating two maxima at 2.35 Å and 2.55 Å.

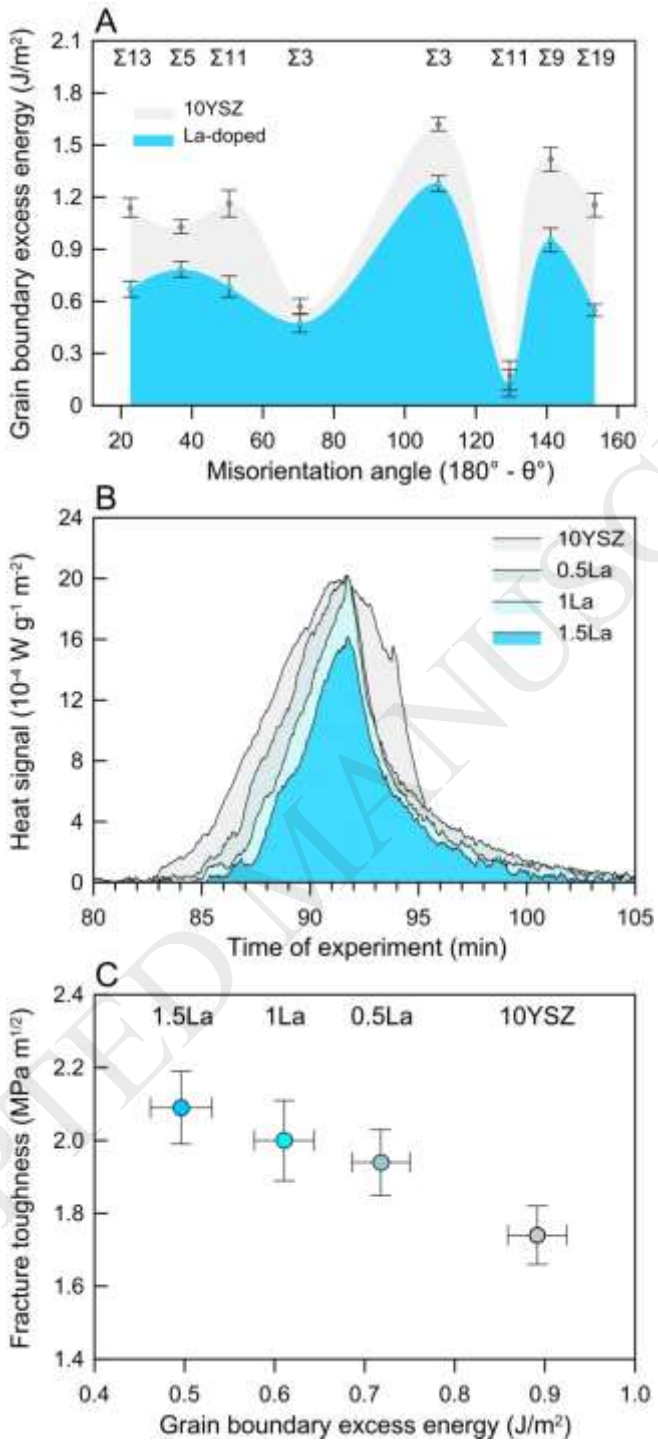


**Fig. 4.** The values of grain boundary excess energy for Σ13, Σ5, Σ11, Σ3, Σ9, Σ19 boundaries (Table 1) as function of misorientation angle for 10YSZ and 1.5La8.5YSZ compositions (A). The DSC curves for 10YSZ and for different La-doping content (B). The correlation between toughness and the average grain boundary excess energy experimentally measured by DSC (C).

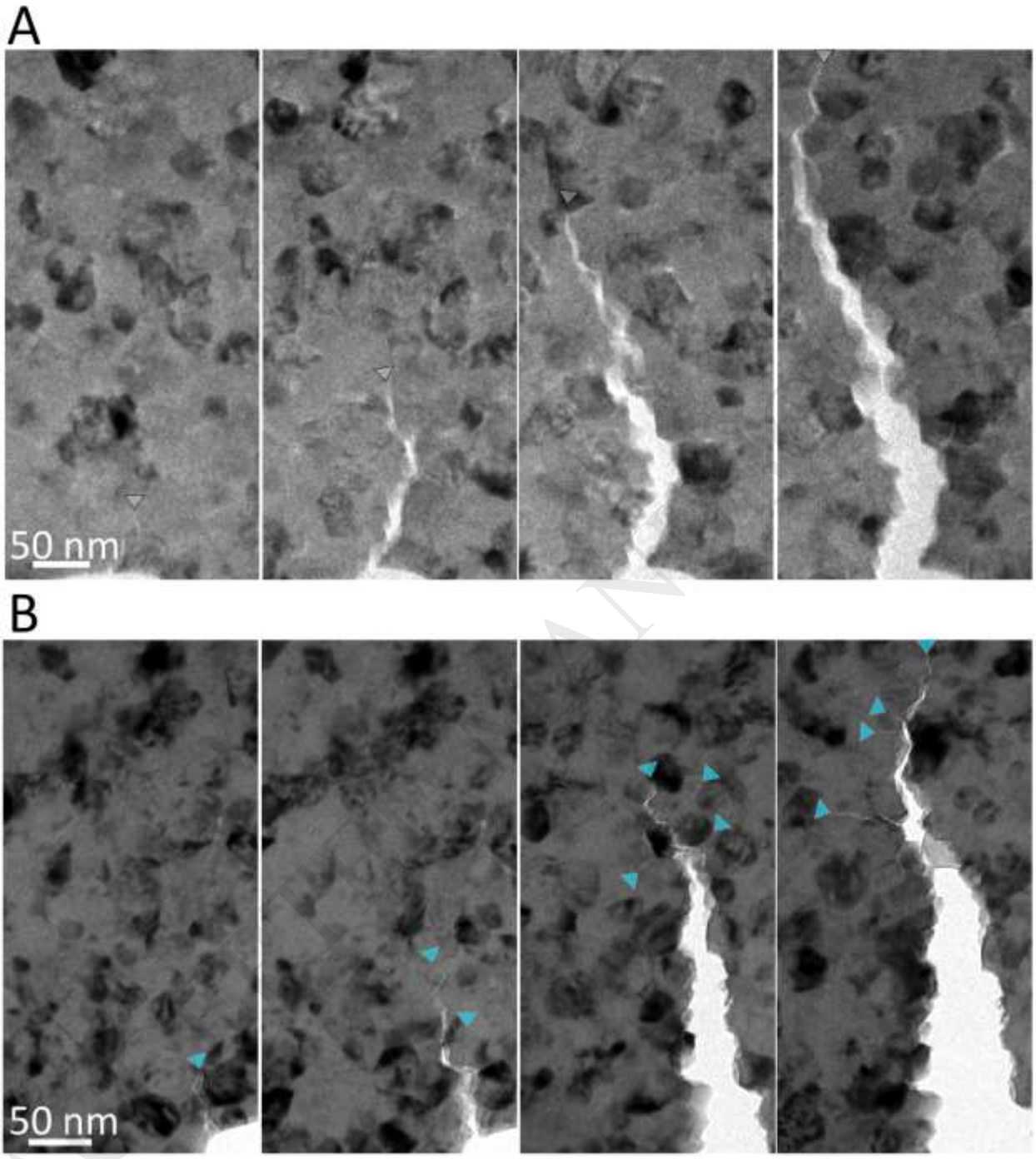


**Fig. 5.** The snapshots of crack propagation in nanocrystalline fully dense YSZ samples. The 10YSZ (A) and 1.5La8.5YSZ (B) have distinct cracking patterns, consistent with deflection and branching caused by the change in grain boundary energy distribution induced by lanthanum doping. The triangles highlight positions of the crack tips.

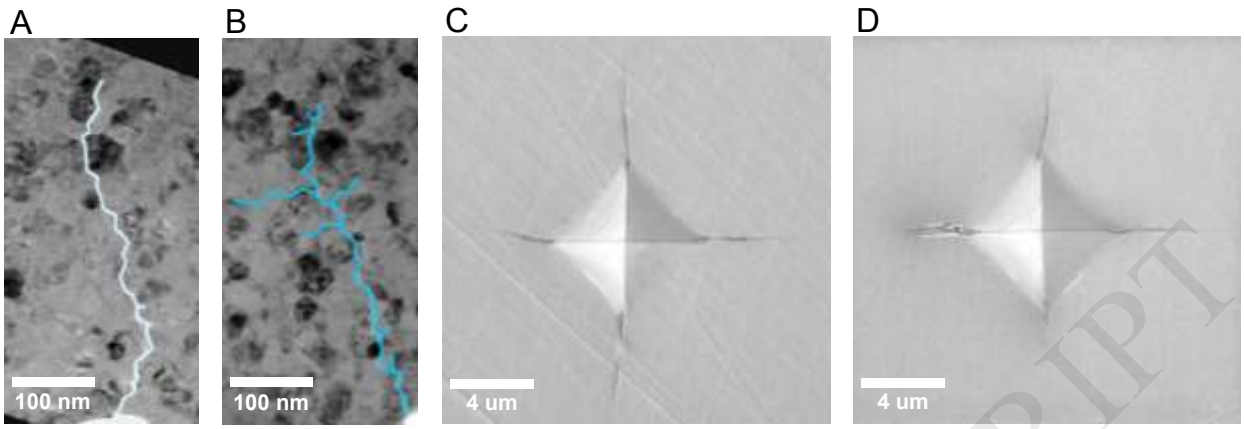


**Fig. 6.** Selected images of tracered cracks observed after in-situ TEM fracture tests in 10YSZ (A) and 1.5La8.5YSZ (B). Selected SEM images of the indentation impressions left by 50gf diamond pyramid on 10YSZ (C) and 1.5La8.5YSZ (D).

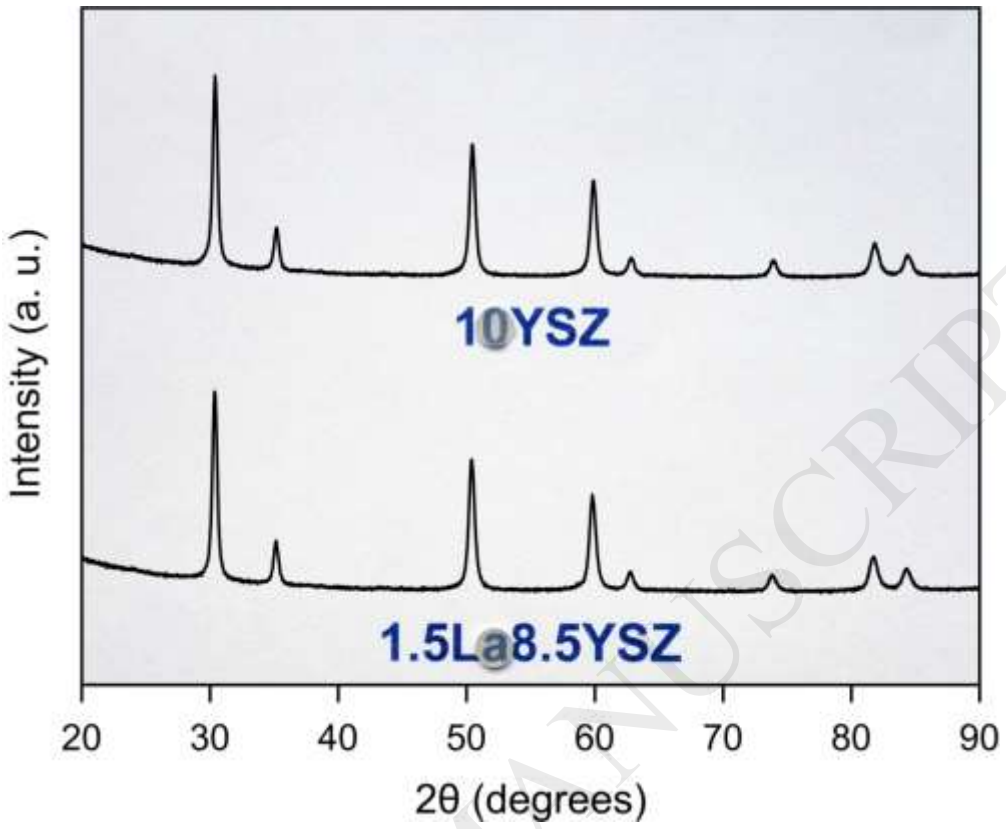


**Fig. 7**. The XRD profiles and photographs (small pellets on top of legends; pellets are 4mm in diameter and ~1mm thick) of 10YSZ and 1.5La8.5YSZ nanocrystalline ceramic samples.

**Table 1.** List of all grain boundaries simulated in this study.

| **Geometry of grain boundary/misorientation angle** | **Size of simulation box $l_x/l_y/l_z$ (Å)** | **Number of atoms in simulation box Zr / O / Y / La substituting Y (if any)** |
|---|---|---|
| [001] tilt axis | | |
| Σ13(510) / 22.62° | 26.08 / 104.26 / 30.77 | 7192 / 2024 / 4720 / 448 |
| Σ5(310) / 36.9° | 32.35 / 64.56 / 30.75 | 5446 / 1532 / 3574 / 340 |
| [110] tilt axis | | |
| Σ11(332) / 50.48° | 24.07 / 102.73 / 28.90 | 6144 / 1728 / 4032 / 384 |
| Σ3(111) / 70.53° | 35.44 / 76.12 / 28.86 | 6703 / 1886 / 4399 / 418 |
| Σ3(112) / 109.47° | 37.54 / 71.49 / 28.90 | 6703 / 1886 / 4399 / 418 |
| Σ11(113) / 129.52° | 33.96 / 98.73 / 28.92 | 8286 / 2332 / 5438 / 516 |
| Σ9(114) / 141.06° | 21.69 / 97.41 / 28.57 | 5120 / 1440 / 3360 / 320 |
| Σ19(116) / 153.47° | 22.34 / 126.85 / 28.96 | 7029 / 1978 / 4613 / 438 |

**Table 2.** The average potential energies in the crystalline lattice for different ions in Σ13 grain boundaries and in the reference bulk phase.

| Type of ion | Average potential energy, eV/atom | | |
|---|---|---|---|
| | **Reference bulk phase of 10YSZ** | **Σ13 grain boundary of 10YSZ** | **Σ13 grain boundary of 1.5La8.5YSZ** |
| $Zr^{4+}$ | -74.67 | -74.45 | -74.50 |
| $Y^{3+}$ | -41.42 | -41.32 | -41.39 |
| $La^{3+}$ | - | - | -38.43 |
| $O^{2-}$ | -18.00 | -18.05 | -18.01 |